Earth Planet. Sci. Lett. 642 (2024) 118867

Contents lists available at ScienceDirect

Earth and Planetary Science Letters

journal homepage: www.elsevier.com/locate/epsl

Low-velocity heterogeneities redistributed by subducted material in the deepest mantle beneath North America

Jonathan Wolf [a,b,*], Mingming Li [c], Maureen D. Long [a]

[a] Department of Earth and Planetary Sciences, Yale University, New Haven, CT, USA
[b] now at: Department of Earth and Planetary Science, University of California, Berkeley, CA, USA
[c] School of Earth and Space Exploration, Arizona State University, Tempe, AZ, USA

ARTICLE INFO

Editor: H. Thybo

Dataset link: https://service.iris.edu

Dataset link: https://service.scedc.caltech.edu

Keywords:
Seismic anisotropy
Geodynamic modeling
Ultralow velocity zones
Lowermost mantle
Slab-driven flow
North America

ABSTRACT

The origins and composition of seismic low-velocity heterogeneities atop the core-mantle boundary (CMB) remain poorly understood. It is also debated whether they are static features or whether they can be displaced and modified by mantle convection, although recent seismological and geodynamic evidence suggests the latter. In this work, we perform the first simultaneous analysis of SPdKS waves to characterize low-velocity heterogeneity and seismic anisotropy, which is evidence for deformation, at the base of the mantle. We find seismic velocity heterogeneity and seismic anisotropy that are co-located with, or adjacent to, each other. Our study region, the lowermost mantle beneath North America, has been shaped by long-term subduction. Through geodynamic modeling simulations, we show that the sinking of subducted slabs to the lowermost mantle can trigger formation of hot thermal anomalies near subducted slabs, where chemical heterogeneities can accumulate. The thermochemical anomalies can cause reduction of seismic velocity while the slab-induced flow can cause seismic anisotropy, potentially explaining our seismic observations.

1. Introduction

The presence of material with extremely low seismic velocities at the base of the mantle was first suggested by Garnero et al. (1993). In the following years, they were named ultralow velocity zones (ULVZs; e.g., Garnero et al., 1998), a name that is still commonly used (e.g., Cottaar and Romanowicz, 2012; Yu and Garnero, 2018; Thorne et al., 2020). However, it is unclear whether the structures referred to as ULVZs are, in fact, all similar in their composition and origin (e.g., Thorne et al., 2021). Moreover, instead of being distinct features, ULVZs may actually be regions of high topography at the top of a thin layer of low velocity and high electrical conductivity at the base of the mantle, which is otherwise challenging to detect seismically (e.g., Buffett et al., 2002; Russell et al., 2022, 2023; Ferrick and Korenaga, 2023). We still do not understand precisely the origin and composition of ULVZs, although various possibilities have been suggested (e.g., Labrosse et al., 2008; Otsuka and Karato, 2012; Lesher et al., 2020; Dobrosavljevic et al., 2019, 2023; Hansen et al., 2023). In particular, more research is needed to conclusively determine whether they are partially molten or solid (e.g., Williams and Garnero, 1996; Lay et al., 2004; Lai et al., 2022).

Crucial for discussions about the origin, composition and general properties of ULVZs is a better understanding of whether they are static features or whether they are influenced by mantle convection. Geodynamic modeling suggests that ULVZs may be transported by mantle flow (e.g., McNamara et al., 2010; Li et al., 2017). Additionally, seismological evidence for co-located ULVZ structure and mantle deformation (as evidenced by seismic anisotropy) has been detected (Wolf and Long, 2023; Wolf et al., 2024a). In one case, the deformation was attributed to a subducted slab remnant at the base of the mantle beneath the Himalayas (Wolf et al., 2024a), consistent with the idea that ULVZs originate from heterogeneous accumulations of previously subducted materials (e.g., Hansen et al., 2023). Therefore, deep mantle heterogeneities may constantly be displaced by mantle flow; this hypothesis, however, requires further observational testing.

Deformation of mantle materials can lead to crystallographic-preferred orientation (CPO) of individual crystals in an aggregate (e.g., Karato et al., 2008), causing seismic anisotropy, which refers to the

* Corresponding author.
E-mail address: jonathan.wolf@yale.edu (J. Wolf).

https://doi.org/10.1016/j.epsl.2024.118867
Received 25 February 2024; Received in revised form 21 June 2024; Accepted 25 June 2024
Available online 4 July 2024

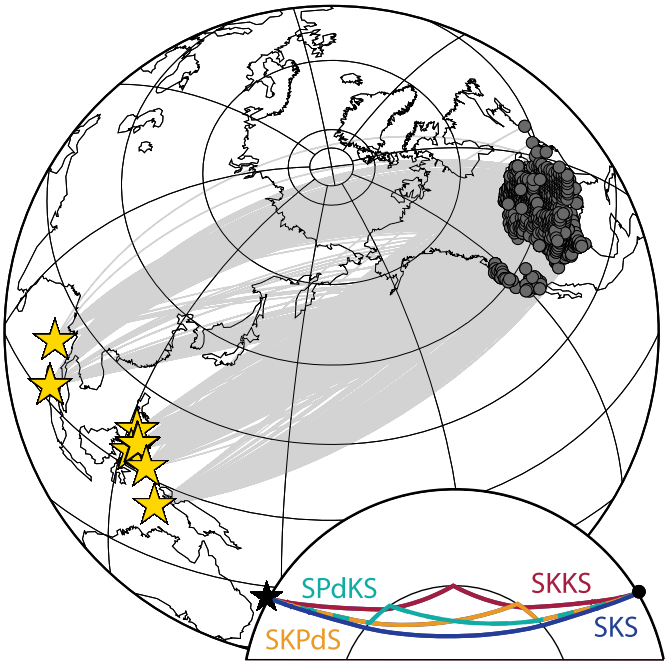

Fig. 1. Source-receiver configuration used in this study. Sources are represented as yellow stars, stations as dark gray circles, and great-circle raypaths as light gray lines. Inset: SKS, SKKS, SPdKS and SKPdS raypaths between source (star) and receiver (circle), shown in a cross-section for a source-receiver distance of 120°.

dependence of propagation velocities on the polarization of the seismic wave (e.g. Nowacki et al., 2011; Romanowicz and Wenk, 2017). Seismic anisotropy manifests in a phenomenon in which seismic shear waves split into a slow and a fast component, called shear-wave splitting (e.g., Silver and Chan, 1991; Long and Silver, 2009). In seismological studies of both velocity heterogeneities and seismic anisotropy, ideally the same seismic waves can be used to find evidence for both. For this reason, previous studies have focused on S_{diff} waves, which sometimes show postcursors that are indicative of ULVZs (e.g., Cottaar and Romanowicz, 2012; Li et al., 2022) but can also be used to measure deep mantle anisotropy under certain conditions (e.g., Cottaar and Romanowicz, 2013; Wolf and Long, 2022; Wolf et al., 2023b).

Another seismic phase that is often used to investigate deep mantle heterogeneity is SPdKS (Fig. 1, inset; e.g., Garnero et al., 1993, Rondenay and Fischer, 2003; Thorne et al., 2020, 2021; Festin et al., 2024). Strictly speaking, SPdKS energy is composed of both SPdKS, which has a diffracted path on the source side, SKPdS, whose diffracted path is on the receiver side, and a combination of both that can be referred to as SPdKPdS (Fig. 1, inset; Thorne et al., 2019). For simplicity, in this work we follow the traditional naming convention and refer to this combined phase as SPdKS, although this is slightly imprecise. Anomalous SPdKS waveforms are often indicative of ULVZ structure in the deepest mantle (e.g., Thorne et al., 2021); however, other types of low-velocity heterogeneity just above the CMB can have similar effects (Garnero and Jeanloz, 2000, Buffett et al., 2002). Therefore, we refer to structure that leads to anomalous SPdKS waveforms using the more general term of lowermost mantle heterogeneity.

SPdKS is sensitive to heterogeneity on the source as well as the receiver side (Fig. 1), which often makes it challenging to pinpoint where exactly mantle heterogeneity is sampled (e.g., Thorne et al., 2020). Thus, it may sometimes be more straightforward to work with other seismic phases, such as S_{diff}; however, worldwide wave sampling strongly depends on the seismic phase used, and S_{diff} sampling is not good everywhere. Besides providing evidence for deep mantle heterogeneity, SPdKS waveforms also contain information about seismic anisotropy, analogous to the commonly used phases SKS and SKKS (Fig. 1, inset). One reason why SPdKS has never been used for the purpose of inferring lowermost mantle anisotropy is likely that its amplitudes are often low at the distances at which SPdKS is clearly separated from SKS.

For the deep mantle beneath North America and the northeastern Pacific Ocean, SPdKS sampling is excellent (Thorne et al., 2021), while S_{diff} sampling is poor (Wolf et al., 2023c). Moreover, the deep mantle beneath North America hosts multiple ULVZs (e.g., Rondenay and Fischer, 2003; Thorne et al., 2019, 2020, 2021), while deformation in this region is dominated by slab remnants, which can lead to strong seismic anisotropy (e.g., Long, 2009; Nowacki et al., 2010; Asplet et al., 2020, 2023; Wolf and Long, 2022; Wolf et al., 2023b). It thus represents an ideal locale to investigate spatial relationships between anisotropy due to slab-driven flow and deep mantle heterogeneity.

In this study, we perform the first joint analysis of SPdKS, SKS and SKKS waves for both deep mantle heterogeneity and anisotropy. Our approach enables us to expand ray coverage, and to determine the location of seismic anisotropy more precisely than previous anisotropy studies that only used SKS and SKKS. We show evidence for two distinct regions of heterogeneity in the deepest mantle, one of which has not been clearly characterized before. These two features, probably ULVZs, are co-located with – or at least in close vicinity to – strong seismic anisotropy. From the results of geodynamic modeling experiments, we suggest that the co-existence of ULVZs and anisotropy in this region can be related to slab-driven flow and formation of thermochemical heterogeneities in the lowermost mantle.

2. Methods

2.1. Measurements of SKS-SKKS-SPdKS differential splitting

A shear wave that travels through an anisotropic medium splits into a fast and a slow component (e.g., Silver and Chan, 1991). The time lag between these two waves is referred to as δt, whereas the polarization direction of the fast traveling component is called ϕ. Sometimes it can be useful to define a third quantity, the splitting intensity (Chevrot, 2000), SI, which can be expressed as:

$$SI = -2\frac{T(t)R'(t)}{|R'(t)|^2} \approx \delta t \sin(2(b-\phi)) \,, \tag{1}$$

where $R'(t)$ is the radial component time derivative, $T(t)$ the transverse component and b denotes the backazimuth. Therefore, SI (measured on an individual seismogram) is large if the transverse component resembles the time derivative of the radial component (which is true for splitting; e.g., Chevrot, 2000) and has a high amplitude.

SplitRacer (Reiss and Rümpker, 2017) incorporates the transverse energy minimization technique (Silver and Chan, 1991) to determine splitting parameters (ϕ, δt) using the corrected uncertainty calculation from Walsh et al. (2013), and also measures SI. When we use SplitRacer to measure SKS and SKKS splitting, we first bandpass-filter our data between 6 and 25 s, only retain data with signal-to-noise ratios (SNRs) > 2, and use 30 random time windows for the splitting analysis. SNRs are calculated comparing the sum of absolute amplitude values for a pre-phase time window with the seismic phase of interest. This procedure is conducted on the effective horizontal component, defined as $\sqrt{(North\ amplitude)^2 + (East\ amplitude)^2}$. For SPdKS, we use the same filter, select those data for which SKS SNRs are > 2, and manually pick the time window that is used to measure splitting. We only measure SPdKS splitting if both the transverse and radial component arrivals are visually distinguishable from the noise, as noise has been shown influence the reliability of SI measurements (e.g., Hein et al., 2021; Wolf et al., 2023a). This implies that, for example, if the SNR of SKS is 2, we only measure SPdKS splitting if its amplitude is close in size to SKS. This, in turn, may result in a disproportional number of SPdKS splitting measurements for phases that are influenced by CMB heterogeneity, because such phases often have larger amplitudes (e.g., Thorne et al., 2020). However, this has no influence on whether the wave is split or not, and

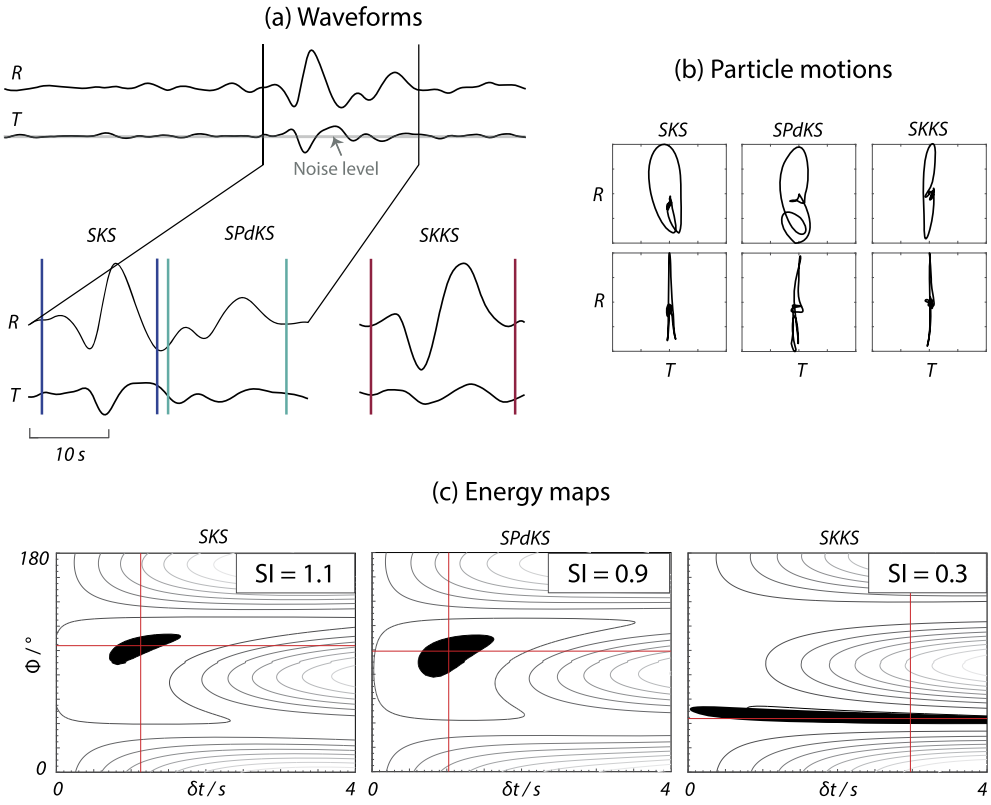

Fig. 2. Example SKS, SPdKS and SKKS splitting measurements for an event that occurred on July 23, 2010 and was recorded at station X33A in the mid southwest United States. (a) Top: 100 s seismogram snippet around the SKS and SPdKS waveforms showing the calculated noise level (gray). Bottom: Radial (R) and transverse (T) velocity seismograms for each phase. Vertical lines indicate the identified time windows for the different phases. (b) Particle motions before (upper row) and after (bottom row) correction for best fitting splitting parameters (for each phase). (c) Energy maps of best fitting splitting parameters (ϕ, δt) for each phase, with black color indicating the 95% confidence region. Splitting intensities are shown in the upper right corners of each individual plot. The SPdKS phase is clearly split, with similar splitting parameters as SKS, whereas SKKS exhibits different behavior, with nearly null splitting.

thus does not influence our interpretations. Due to possible phase interference of SKS, a strategy of multiple random time window selections, which is often used in shear wave splitting studies, is not practical for SPdKS.

The measurement of differential SKS-SKKS splitting is often interpreted as evidence for lowermost mantle anisotropy (e.g., Niu and Perez, 2004; Long, 2009; Deng et al., 2017; Reiss et al., 2019; Grund and Ritter, 2019). The reason is that SKS and SKKS raypaths in the upper mantle are almost identical, while they have a much larger spatial separation in the lowermost mantle (Fig. 1, inset). Because the bulk of the lower mantle is almost isotropic (e.g., Meade et al., 2005; French and Romanowicz, 2014), substantial differences in shear-wave splitting due to seismic anisotropy must therefore be accumulated on the deep mantle portions of the raypaths. Global wavefield simulations have confirmed the reliability of this approach if SI differences > 0.4 are interpreted as being indicative of an anisotropy contribution from the deep mantle (Tesoniero et al., 2020; Wolf et al., 2022). In this work, we expand this technique to SPdKS phases, whose S raypath through the receiver-side lower mantle is similar to SKS, and substantially differs from SKKS (Fig. 1, inset). We therefore expect that SKS-SPdKS SI differences will be relatively low, while they will be larger for SKKS-SPdKS in places in which lowermost mantle anisotropy is present.

For the measurement of SKS-SKKS differential splitting, seismograms recorded at epicentral distances between 108° and 122° are often used (e.g., Wolf et al., 2024b), although there is technically no upper distance limit as long as splitting measurements from both SKS and SKKS are robust. In this work, we face the challenge that SKS and SPdKS amplitudes generally die off quickly at large distances ($> 115°$), while SKS and SPdKS only have clearly distinguishable arrivals for distances $> 120°$. This influences our event selection: We only select events that have sufficiently large SKS and SPdKS amplitudes (compared to the noise level) at distances $> 120°$ and, thus, enable shear-wave splitting measurements for both phases. If this condition is met, the SKKS signal clarity is also usually sufficient. Overall, we find 10 events (Supplementary Table S1), recorded at stations in the contiguous United States, that generally fit these criteria (Fig. 1). We measure SKS-SKKS differential splitting at epicentral distances between 108° and 135° and differential SKS/SKKS-SPdKS splitting between 120° and 135°. An example for the measurement of SKS, SKKS, and SPdKS splitting on the same seismogram is shown in Fig. 2. In this example, SKS-SPdKS splitting is nondiscrepant ($\delta SI < 0.4$), while both SKKS-SPdKS and SKS-SKKS differential splitting are discrepant ($\delta SI > 0.4$).

2.2. Heterogeneity detection using SPdKS

The explanation that was first invoked for anomalous SPdKS waveforms was the presence of ULVZ structure (Garnero et al., 1993). However, besides distinct low-velocity patches, a gradational boundary between core and mantle (Garnero and Jeanloz, 2000) can also potentially explain anomalous SPdKS observations. Despite these different possible explanations, heterogeneity locations suggested using SPdKS agree very well with ULVZ locations inferred using different seismic phases such as ScP, S_{diff} and PcP (e.g., Yu and Garnero, 2018; Thorne et al., 2021). Therefore, it is likely that the deep mantle heterogeneity that we investigate is identical to what is commonly referred to as ULVZ structure, although we cannot be fully certain.

Thorne et al. (2020) conducted detailed global wavefield simulations to investigate the conditions under which SPdKS waves are indicative of anomalous deep mantle structure. Following this previous work, we define SPdKS waveforms as anomalous if 1) they show two distinct

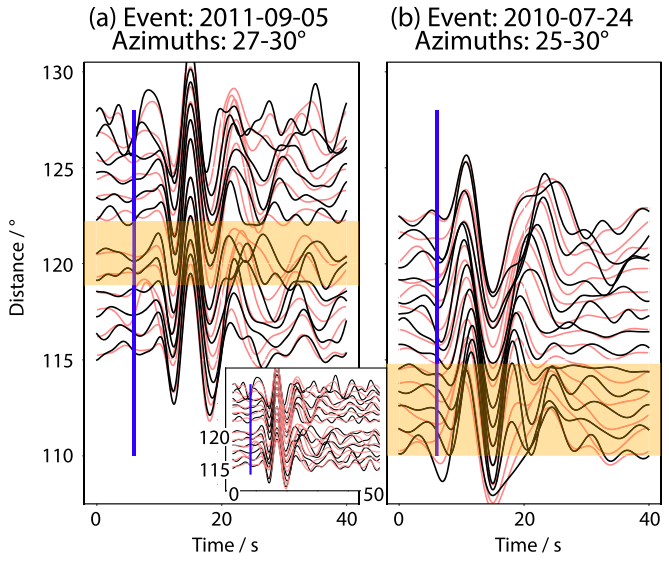

Fig. 3. Real (black) and synthetic (red) radial velocity seismogram stacks for 1° distance bins for two example events that show anomalous SPdKS arrivals. (a) The blue line indicates the approximate SKS arrival time. Yellow shading indicates distance range associated with pulse splitting for the real data caused by anomalous SPdKS waves, which is not observed for the synthetics. Inset: Same representation for a longer time interval. No SKiKS arrival is apparent (that could be an alternative cause for the observed waveform anomalies). Seismograms are from an event that occurred on September 5, 2011, with waveforms recorded at azimuths 27 to 30°. (b) Same as panel (a) for an event that occurred on July 5, 2010, recorded at azimuths 25 to 30°.

SKS/SPdKS arrivals where synthetic seismograms calculated for PREM only predict one (Fig. 3), and 2) the amplitude of the second arrival is comparable to, or larger than, the first. We additionally define SPdKS as anomalous if we can detect a distinct SPdKS pulse that is clearly delayed compared to what is expected from the synthetics, although none of the seismic waves for which this last definition was used plays a role in our interpretation (for reasons laid out in Section 3.2). We conduct this analysis using seismograms that are stacked in 1° distance bins, and only characterize SPdKS as anomalous (or not) if noise levels allow the clear detection of SPdKS signals (Fig. 3). We place particular emphasis on avoiding the misinterpretation of SKiKS waves as SPdKS at distances around 120° (Fig. 3a). Synthetic wavefield simulations (down to 3 s) are conducted with AxiSEM3D (Leng et al., 2016, 2019) using PREM (Dziewonski and Anderson, 1981) as a background model, including attenuation and ellipticity.

3. Results

3.1. Lowermost mantle anisotropy

Fig. 4 shows spatially binned splitting intensity results (for results without binning, see Supplementary Figure S1). We find strong SKS-SKKS differential splitting for raypaths that sample the deep mantle beneath the northeastern Pacific Ocean, while splitting is mostly nondiscrepant beneath the parts of the United States and Canada that are within our study region (Fig. 4a). Exceptions, in which differential splitting is strong, include the westernmost part of Canada and parts of the southwestern United States (Fig. 4a). These results generally agree with previous work that investigated SKS-SKKS differential splitting for some parts of the region under study (e.g., Long, 2009; Asplet et al., 2020; Wolf et al., 2024c). SKS-SPdKS differential splitting is largely nondiscrepant (Fig. 4b). The bins to the east that show moderate discrepancies are only influenced by a few measurements (Supplementary Figure S1) and are therefore less trustworthy than most other bins. The finding of weak SKS-SPdKS differential splitting is what we expect. The reason is that SKS and SPdKS raypaths are almost identical throughout the whole mantle (Fig. 1), and should therefore sample very similar seismic anisotropy. The pattern of SKKS-SPdKS splitting discrepancies, on the other hand, is very similar to SKS-SKKS differential splitting, although fewer regions are sampled. Our general finding of small SI discrepancies between SKS-SPdKS and larger discrepancies between SKS-SKKS and SKKS-SPdKS agrees with our expectation based on their deep mantle raypaths.

3.2. Potential heterogeneity locations

We detect anomalous SPdKS waveforms (Section 2.2) at multiple backazimuthal swaths. Fig. 5a shows P_{diff} raypaths of SPdKS on source and receiver side, with path color indicating whether SPdKS phases are anomalous or not. The background colors in Fig. 5a show the likelihood of heterogeneity determined by Thorne et al. (2021), who argued that the most parsimonious heterogeneity distribution inferred from SPdKS would be the most likely. This argument takes into consideration the source-receiver side ambiguity of possible heterogeneity locations inferred from SPdKS. It is furthermore based on the observation that in case of source-side heterogeneity, SPdKS waveforms are anomalous for a much larger backazimuthal swath than for heterogeneity located on the receiver side. While this is not necessarily true in every single case, Thorne et al. (2021) successfully reproduced known ULVZ locations that had been found using independent approaches, indicating the general validity of this assumption. However, it is worth pointing out that the probabilities obtained by Thorne et al. (2021) appear to be underestimated, as ULVZs have indeed been observed in most regions with probabilities ~25 % using independent methods.

Following the arguments from Thorne et al. (2021), we do not interpret anomalous SPdKS waveforms as indicative of receiver-side heterogeneity if the same anomalous waveform features occur across a more than 10° wide backazimuthal swath. The P_{diff} portions of the SPdKS raypaths with these characteristics are shown in orange in Fig. 5a. We cannot confidently infer whether these waveform anomalies are due to source-side heterogeneity as opposed to receiver-side heterogeneity – we simply do not form an opinion. Interestingly, however, the source-side P_{diff} raypath legs for which SPdKS waveform anomalies can be identified for a large backazimuthal swath do consistently sample regions on the source side for which large heterogeneity probabilities were inferred by Thorne et al. (2021).

The two types of anomalous waveform features shown in Fig. 3 only occur in a relatively tight backazimuthal range ($\leq 5°$) and are therefore strong candidates as features caused by heterogeneity along the P_{diff} raypath leg of SPdKS on the receiver side. The feature shown in Fig. 3a is clearly visible for one other event with a similar epicenter, while the other feature (Fig. 3b) can be observed for three other events that occurred at a similar location. Fig. 5b shows all the receiver-side P_{diff} raypath segments for these two anomalous backazimuthal swaths. Paths A and B correspond to the waveform features shown in Fig. 3a and b. The source-side P_{diff} raypaths corresponding to Path A cross a region with a heterogeneity likelihood of ~15 % in the study of Thorne et al. (2021), while the source-side heterogeneity likelihood is larger (~20 – 25 %) for raypaths at slightly smaller and larger backazimuths, which do not show anomalies. Following this line of reasoning, if the observed waveform features were caused by source-side structure, we would expect them to occur across a larger backazimuthal swath. On the receiver side, Path A goes across a region with heterogeneity probabilities of over 20 %. This feature was shown in Thorne et al. (2020, 2021), but not conclusively found to be a deep mantle heterogeneity location. Taking all aforementioned evidence into account, we suggest that our anomalous SPdKS waveforms on Path A are indeed caused by this (previously uncharacterized) heterogeneity on the receiver side. Importantly, Path A does not cross the ULVZ structure found by Revenaugh and Meyer (1997) in the northeastern Pacific.

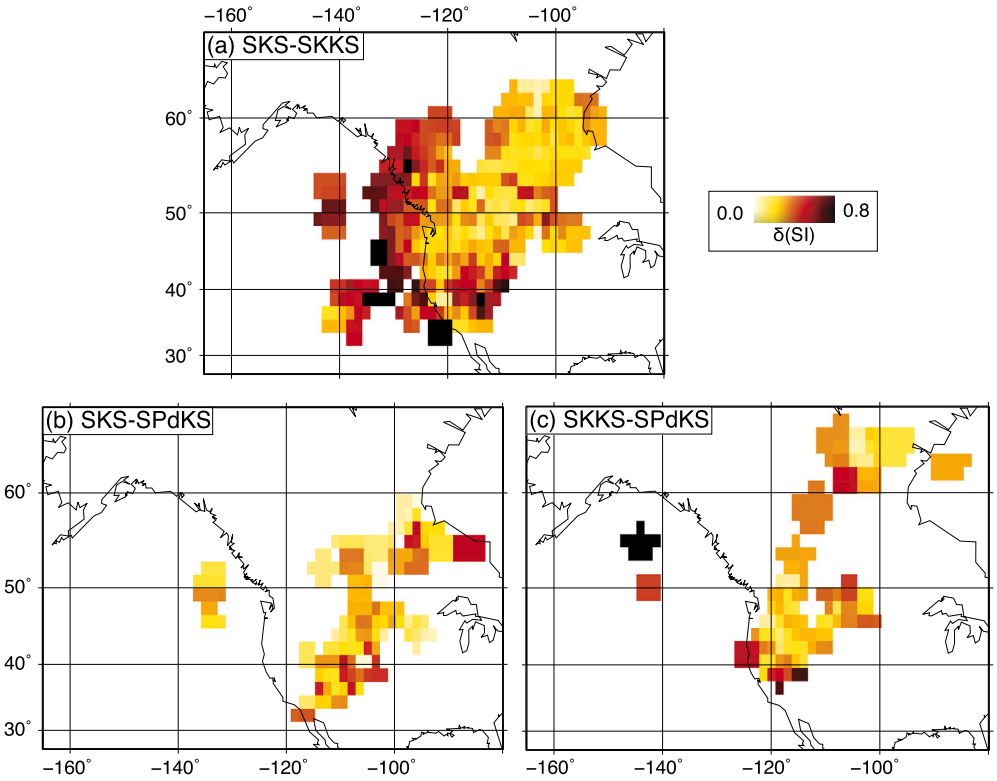

Fig. 4. Average splitting intensity discrepancies (see legend) for 1.5° × 1.5° sized bins for (a) SKS-SKKS, (b) SKS-SPdKS and (c) SKKS-SPdKS differential splitting.

The source-side P_{diff} raypath segments corresponding to Path B sample a region with a heterogeneity probability > 50 %, while the probability is similarly high on the receiver side. If the potential ULVZ on the source side was responsible for the anomalous waveform features, we would expect the waveform anomalies to occur in a larger backazimuthal range, given the size of the source-side high-probability region. In contrast, Path B samples the exact region of high heterogeneity probabilities on the receiver side. Close to this region, ULVZ structure was also suggested by Rondenay and Fischer (2003) based on observations of SPdKS phases. We therefore find it more likely that the Path B waveform features are due to receiver-side rather than source-side heterogeneity. However, we make this statement with a lower level of certainty than for the heterogeneity located along Path A. In any case, since the independent results of Rondenay and Fischer (2003) and Thorne et al. (2021) indicate ULVZ structure in this region, it is not crucial for our interpretation to have identified this structure ourselves based on SPdKS waves.

In this study, we do not focus on the precise properties of the detected wavespeed anomalies. However, it has been shown in previous work that waveform and travel time anomalies such as those observed in this study cannot be explained by moderate velocity reductions of a few per cent (e.g., Garnero and Helmberger, 1998). Typically, strong (> 10 %) P wave reductions, and even more extreme reductions in shear velocities (~20 % to 50 %) are invoked (Thorne et al., 2020; Festin et al., 2024). Therefore, strong heterogeneity is required to explain our seismic observations, as further discussed in Section 4.

4. Geodynamic interpretation

We have identified regions with strong deep mantle anisotropy (Fig. 4) and likely low-velocity heterogeneity (Fig. 5) just above the CMB. The heterogeneity locations coincide with, or are adjacent to, locations of strong deep mantle anisotropy (Fig. 6a). Additionally, we find strong seismic anisotropy close to the location beneath northern Mexico and the southern United States at which Thorne et al. (2021) show a high probability of heterogeneity (Fig. 5). This location, while not well-sampled by SPdKS in this study, was also found to host ULVZ structure by Thorne et al. (2019) (Fig. 5b) and Havens and Revenaugh (2001). All these potential heterogeneity locations are characterized by above-average background seismic velocities (Fig. 6b), some of which were identified by van der Meer et al. (2018) as ancient subducted anomalies, specifically the Beaufort and Wichita slabs (Fig. 6b). The origin of another high-velocity anomaly beneath the northeastern Pacific Ocean is unclear, although its shape can potentially be explained by subducted slabs piling up at the CMB (Fig. 6c). This possibility is also supported by global seismic tomography models, which consistently show substantially higher than average seismic velocities at the base of the mantle beneath the northeastern Pacific Ocean and the northwestern United States (e.g., Simmons et al., 2010; Ritsema et al., 2011; French and Romanowicz, 2014).

To better understand the co-existence of ULVZs and seismic anisotropy beneath subduction region, we perform 3D thermochemical calculations to study the dynamics of subducted slabs and their influence on mantle flow and thermal and chemical structure in the lowermost mantle. Our model has a similar setup as that in Li (2023) and is built from the case 1 of Li (2023). The model uses a 3D spherical geometry that covers the whole mantle depth and has a lateral dimension of 120° (longitudinal) × 60° (latitudinal) (Fig. 7a). The surface is divided into an overriding plate and a subducting plate, and asymmetric subduction is achieved by imposing a constant westward velocity of 3 cm/yr of the subducting plate at the surface (Li, 2023). A 10-km-thick oceanic crust is employed at the top of the subducting plate. The oceanic crust is 2% intrinsically denser than background mantle, which falls within the range of density difference between basalt and pyrolite as constrained in mineral physics experiments (e.g., Ringwood, 1990; Hirose et al., 2005). The oceanic crust sinks to the deep mantle with the subducting plate. The viscosity is both temperature and pressure dependent and is expressed as $\eta = \eta_r exp[A(0.6 - T)]$, where A is activation energy that controls temperature-dependence of viscosity, T is non-dimensional temperature, and η_r is a prefactor that controls depth-dependence of viscosity. In this model, $A = 6.91$ in hot regions with $T \geq 0.6$ and $A = 11.51$ in cold regions with $T < 0.6$. The η_r is 1.0 and 30.0 in the upper mantle and

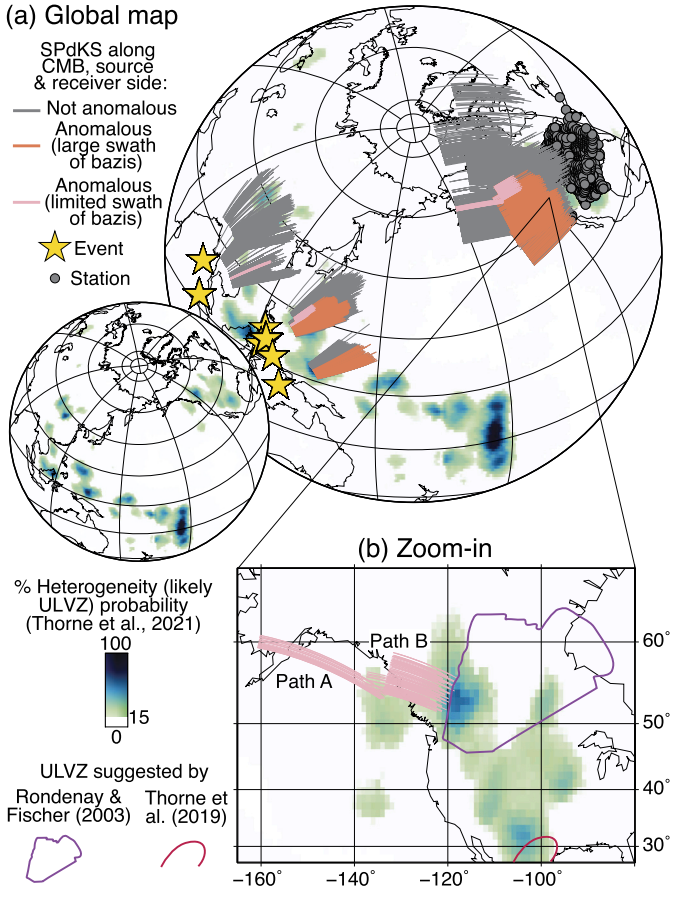

Fig. 5. Heterogeneity results obtained using SPdKS phases. (a) Sources are represented as yellow stars, stations as dark gray circles, and possible raypaths of SPdKS along the CMB on source and receiver side as gray (not anomalous), orange (anomalous for backazimuthal swath $\geq 10°$) and pink (anomalous for backazimuthal swath $\leq 5°$) lines (see legend). Background colors represent heterogeneity (likely ULVZ) probabilities calculated by Thorne et al. (2021) (see legend). (b) Similar plotting conventions as for panel (a) for a zoomed-in geographical region and showing a more limited set of data. Paths along which SPdKS waves are likely influenced by receiver-side heterogeneity (see text) are shown in pink and labeled Path A and Path B. ULVZ locations suggested by Rondenay and Fischer (2003) and Thorne et al. (2021) are outlined in violet and red respectively.

lower mantle, respectively, leading to a 30 times viscosity jump from upper mantle to lower mantle. Due to the temperature dependence of viscosity, the cold subducted slab is more viscous than the surrounding mantle. More details of model setup are presented in Li (2023). Different from models in Li (2023), a layer of another chemical component is imposed in the lowermost 5 km of the mantle, representing products of core-mantle reaction (e.g., Loper and Lay, 1995; Otsuka and Karato, 2012; Lai et al., 2022) and is assigned the same intrinsic density as the oceanic crust.

We find that as the subducting slab reaches the base of the mantle, its motion changes from being mainly vertical to mainly horizontal (Fig. 7a), which can lead to slab deformation. The transition to horizontal flow in the lowermost mantle observed in the geodynamic model is supported by seismic anisotropy studies, which show that our study region is broadly dominated by higher shear velocities for horizontally than vertically traveling shear waves (e.g., Panning and Romanowicz, 2006; French and Romanowicz, 2014). If seismic anisotropy is due to shape-preferred orientation, this observation implies horizontal rather than vertical flow (e.g., Kendall and Silver, 1998; Yamazaki and Karato, 2007). For the case of seismic anisotropy due to the alignment of individual crystals in an aggregate (crystallographic-preferred orientation), multiple studies have shown that a horizontal flow geometry plausibly explains measured shear-wave splitting parameters in this region (e.g., Wolf and Long, 2022; Asplet et al., 2023). These previous studies that suggested flow directions for parts our study region did not (only) rely on differential *KS splitting measurements, which made it possible to infer flow. The differential SKS-SKKS and SPdKS-SKKS splitting measurements made in this study are an excellent seismic anisotropy detector. However, they are unsuitable to infer deep mantle flow directions, because it is generally unclear which phase(s) are influenced by lowermost mantle anisotropy, and to what degree (e.g., Wolf et al., 2024b). It is thus not possible to estimate splitting parameters due to lowermost mantle anisotropy for individual raypaths using this approach. Therefore, for our interpretation, we focus on a qualitative comparison of seismic anisotropy and geodynamic modeling results.

We also find that the subducted slab is sometimes folded in the lowermost mantle (Supplementary Movie S1) in our models, which may result in additional slab deformation. Note that folding behavior of subducted slabs in the lowermost mantle has been inferred using seismic observations as well (e.g., Hutko et al., 2006). Previous numerical modeling experiments that combine mantle convection and mineral physics elasticity have shown that CPO can develop due to slab deformation, causing strong seismic anisotropy in the D″ layer (McNamara et al., 2002, 2003). Therefore, the strong seismic anisotropy in our study region can be explained by flow and deformation caused by subducted slabs. Our model also shows that the arrival of the subducted slab to the lowermost mantle and its changes of morphology by folding are often accompanied by the formation of hot thermal anomalies near the slab (Fig. 7a; Supplementary Movie S1). The radial flow velocity increases in the hot anomalies, which may cause additional deformation and thus increase the magnitude of anisotropy.

Models with different viscosity structures than that shown in Fig. 7 are presented in Li (2023). We find that once the slab arrives at the lowermost mantle, the change of flow direction from being mostly vertical to mostly lateral is independent of modeling parameters, which is not surprising because the CMB is a physical barrier that stops vertical advection between core and mantle. However, the folding behavior of subducted slabs strongly depends on slab viscosity. As slab viscosity in the lowermost mantle is reduced, for example, by either reducing the degree of temperature-dependence of viscosity and/or by reducing the viscosity of postperovskite (Ppv), slabs fold less frequently (Li, 2023). Despite that, hot upwelling plumes still form in regions adjacent to subducted slabs in the lowermost mantle (Li, 2023). The formation of hot thermal anomalies in subduction regions of the lowermost mantle may be triggered due to the arrival of cold subducted slabs or the result of small-scale convection (Li, 2020).

The most widespread mineral in the lowermost mantle is bridgmanite and its high-pressure polymorph Ppv (e.g., Trønnes, 2010). Due to the above average shear velocities in most of our study region, implying lower than average temperatures and a relatively shallow bridgmanite-postperovskite transition (e.g., Murakami et al., 2004), Ppv may dominate. This has also been suggested based on modeling of seismic anisotropy measurements conducted in previous studies (e.g., Wolf and Long, 2022; Asplet et al., 2023). Therefore, at least in parts of our study region, the measured deep mantle anisotropy may be due to CPO of Ppv. Additionally, it has also been argued that thin lenses of Ppv may exist near the CMB in some regions (e.g., Hernlund et al., 2005), which could cause seismic anisotropy due to SPO. While our observations of seismic anisotropy cannot distinguish between these scenarios, they would not generally lead to wavespeed heterogeneities sufficient to cause SPdKS waveform anomalies (e.g., Thorne et al., 2020).

As subducted slabs reach the lowermost mantle, they are warmed up and become less viscous, which facilitates the segregation of subducted oceanic crust from the relatively cold slab. The segregation of subducted oceanic crust is greatly controlled by (and increases with) its thickness

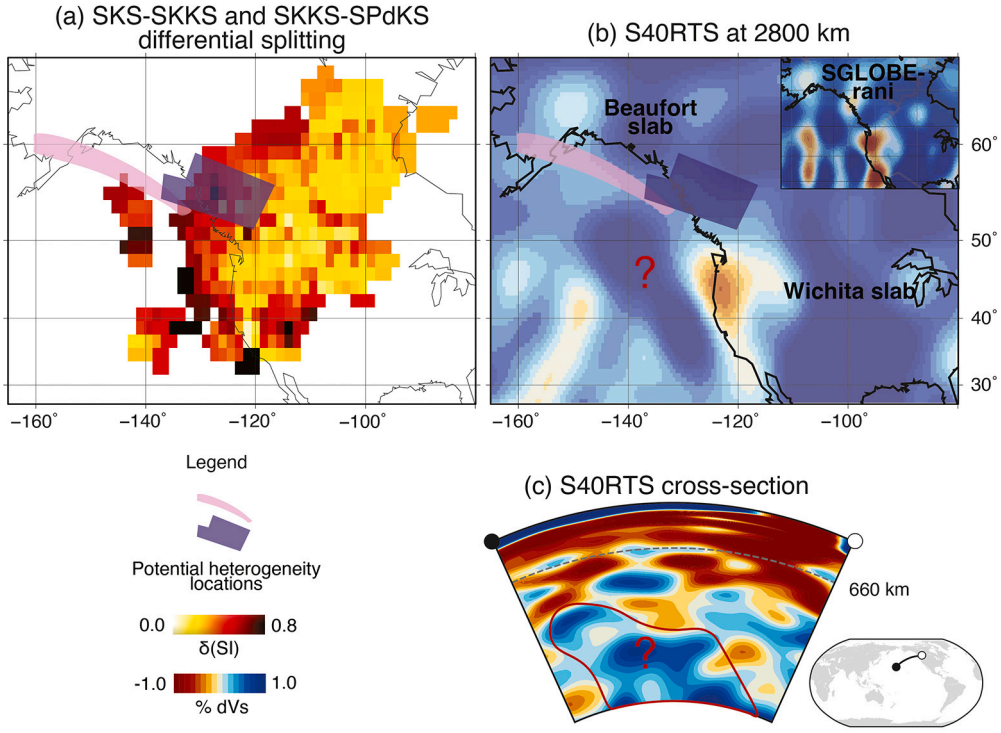

Fig. 6. Summary of seismological results. (a) Combined SKS-SKKS and SKKS-SPdKS differential splitting measurements using the same plotting conventions as in Fig. 4a. Candidate heterogeneity locations are shown in pink and violet shading (see legend). (b) Velocity perturbations for the S40RTS (Ritsema et al., 2011) tomography model and candidate heterogeneity locations (see legend). Previously identified slab remnants (van der Meer et al., 2018) are labeled. An unidentified high-velocity patch is marked by the red question mark. The inset shows velocity perturbations for the same region using the SGLOBE-rani (Chang et al., 2015) tomography model for comparison. (c) S40RTS cross-section examining the unidentified high-velocity patch (red question mark) for the start-end points shown at bottom right. Connected high-velocity structure is shown that could potentially be a subducted slab remnant. Inset shows cross-section location.

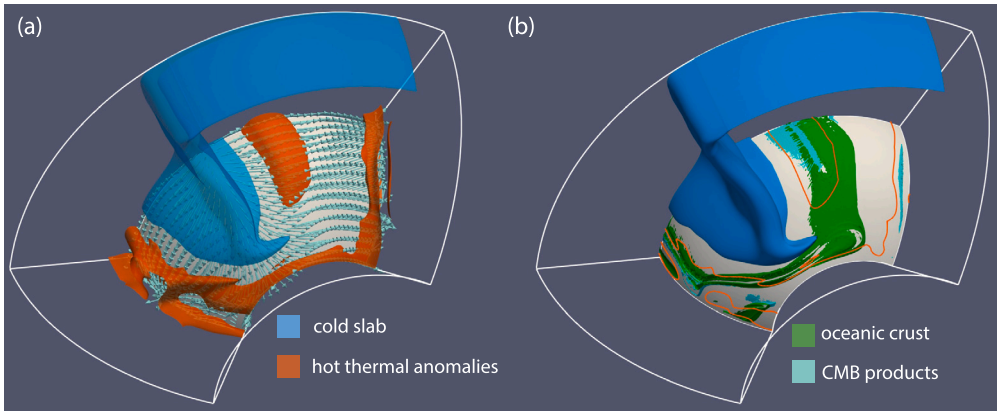

Fig. 7. (a) Snapshot of temperature field in the geodynamic model, showing the subducted slab (blue) and hot thermal anomalies (red). The arrows show mantle flow velocity at 50 km above the CMB. (b) Snapshot of compositional field in the geodynamic model, showing accumulations of oceanic crust (green) and products of core-mantle reaction (cyan) on the CMB. The red contours are at temperatures of 125 K higher than horizontal average, showing locations of hot thermal anomalies at this depth. In both panels, the gray color shows the CMB, and the white lines show the boundaries of the model domain.

and intrinsic density anomaly. Crustal segregation is also observed in our model in this study (Fig. 7b). We find that the crustal accumulations often occur in the hot thermal anomalies (Fig. 7b). Due to its relatively low melting temperature (e.g., Andrault et al., 2014), the oceanic crust in the hot thermal anomalies could be partially molten, causing ULVZs. Additionally, water and other incompatible elements may be present at the CMB (e.g., Ko et al., 2022), possibly transported downwards in slabs (e.g., Walter, 2021), causing reduced melting temperatures of deep mantle materials. Therefore, the co-existence of seismic anisotropy and ULVZs in our study region can be both related to the subduction of slab to the lowermost mantle. Alternatively, or in addition to, subducted oceanic crust, products of core-mantle reaction also preferentially accumulate in the hot thermal anomalies in the lowermost mantle (Fig. 7b). These products may contribute to ULVZ formation as well, although their volume remains uncertain due to poorly constrained rates of core-mantle reactions in the real Earth. Therefore, it is plausible that either the observed strong seismic wavespeed heterogeneity is caused by accumulations of subducted material, or that the downwelling material leads to the accumulation of pre-existing CMB material in seismically visible patches. Given the necessity for large velocity reductions to explain our seismic observations, it appears unlikely that our observations can be explained solely by hot thermal anomalies without chemical heterogeneity.

5. Summary

In this work, we have conducted the first (to our knowledge) simultaneous analysis of SPdKS waves for both deep mantle anisotropy and low velocity heterogeneity. We have found evidence for likely ULVZ structure in the lowermost mantle beneath North America and the northeastern Pacific Ocean. Multiple ULVZ locations beneath North America are co-located with, or adjacent to, strong seismic anisotropy, likely caused by slab-driven flow. Through geodynamic modeling simulations, we find that the sinking of subducted slabs into the lowermost mantle can trigger the development of hot thermal anomalies adjacent to these slabs. These hot anomalies serve as sites where chemical heterogeneities such as subducted oceanic crust and products of core-mantle reaction can accumulate. Consequently, these thermochemical anomalies induce strong reductions in seismic velocity, while the flow induced by the descending slabs leads to seismic anisotropy, providing an explanation for our seismic observations.

Code availability

The synthetic seismograms for this study were computed using AxiSEM3D (Leng et al., 2016, 2019), which is publicly available at https://github.com/AxiSEMunity and described in detail in Fernando et al. (2024).

CRediT authorship contribution statement

Jonathan Wolf: Writing – review & editing, Writing – original draft, Visualization, Validation, Software, Methodology, Investigation, Data curation, Conceptualization. **Mingming Li:** Writing – review & editing, Writing – original draft, Visualization, Methodology, Investigation, Conceptualization. **Maureen D. Long:** Writing – review & editing, Supervision, Resources, Conceptualization.

Declaration of competing interest

The authors are not aware of any competing financial or personal interests that could have influenced the work reported in this paper.

Data availability

We downloaded data with network codes AZ (UC San Diego, 1982), BK (Northern California Earthquake Data Center, 2014), CI (California Institute of Technology and United States Geological Survey Pasadena, 1926) and TA (IRIS Transportable Array, 2003). These data are publicly available at the SAGE DMC Archive (https://service.iris.edu/) and SCEDC (https://service.scedc.caltech.edu).

Acknowledgements

This work was funded by Yale University, by NSF grants EAR-2216564 and EAR-2054926 to ML, and by NSF grant EAR-2026917 to MDL. The Generic Mapping Tools (Wessel and Smith, 1998), TauP (Crotwell et al., 1999), ObsPy (Beyreuther et al., 2010) and SplitRacer (Reiss and Rümpker, 2017) were used in this research. We are grateful to Ed Garnero and Annie Haws for helpful discussions. We thank Mike Thorne for making the heterogeneity probability map from Thorne et al. (2021) publicly available. We are thankful to Philip Crotwell, who made a beta TauP version available before its official release, including improvements that helped in this work. We thank Zhouchuan Huang and an anonymous reviewer for thoughtful reviews.

Appendix A. Supplementary material

Supplementary material related to this article can be found online at https://doi.org/10.1016/j.epsl.2024.118867.

References

Andrault, D., Pesce, G., Bouhifd, M.A., Bolfan-Casanova, N., Hénot, J.M., Mezouar, M., 2014. Melting of subducted basalt at the core-mantle boundary. Science 344, 892–895. https://doi.org/10.1126/science.1250466.

Asplet, J., Wookey, J., Kendall, M., 2020. A potential post-perovskite province in D″ beneath the Eastern Pacific: evidence from new analysis of discrepant SKS–SKKS shear-wave splitting. Geophys. J. Int. 221, 2075–2090. https://doi.org/10.1093/gji/ggaa114.

Asplet, J., Wookey, J., Kendall, M., 2023. Inversion of shear wave waveforms reveal deformation in the lowermost mantle. Geophys. J. Int. 232, 97–114. https://doi.org/10.1093/gji/ggac328.

Beyreuther, M., Barsch, R., Krischer, L., Megies, T., Behr, Y., Wassermann, J., 2010. ObsPy: a Python toolbox for seismology. Seismol. Res. Lett. 81, 530–533. https://doi.org/10.1111/10.1785/gssrl.81.3.530.

Buffett, B.A., Mathews, P.M., Herring, T.A., 2002. Modeling of nutation and precession: effects of electromagnetic coupling. J. Geophys. Res., Solid Earth 107, ETG 5-1–ETG 5-14. https://doi.org/10.1029/2000JB000056.

California Institute of Technology and United States Geological Survey Pasadena, 1926. Southern California Seismic Network. https://doi.org/10.7914/SN/CI.

Chang, S.J., Ferreira, A.M.G., Ritsema, J., van Heijst, H.J., Woodhouse, J.H., 2015. Joint inversion for global isotropic and radially anisotropic mantle structure including crustal thickness perturbations. J. Geophys. Res., Solid Earth 120, 4278–4300. https://doi.org/10.1002/2014JB011824.

Chevrot, S., 2000. Multichannel analysis of shear wave splitting. J. Geophys. Res., Solid Earth 105, 21579–21590. https://doi.org/10.1029/2000JB900199.

Cottaar, S., Romanowicz, B., 2012. An unusually large ULVZ at the base of the mantle near Hawaii. Earth Planet. Sci. Lett. 355–356, 213–222. https://doi.org/10.1016/j.epsl.2012.09.005.

Cottaar, S., Romanowicz, B., 2013. Observations of changing anisotropy across the southern margin of the African LLSVP. Geophys. J. Int. 195, 1184–1195. https://doi.org/10.1093/gji/ggt285.

Crotwell, P., Owens, T.J., Ritsema, J., 1999. The TauP toolkit: flexible seismic travel-time and raypath utilities. Seismol. Res. Lett. 70. https://doi.org/10.1785/gssrl.70.2.154.

Deng, J., Long, M.D., Creasy, N., Wagner, L., Beck, S., Zandt, G., Tavera, H., Minaya, E., 2017. Lowermost mantle anisotropy near the eastern edge of the Pacific LLSVP: constraints from SKS-SKKS splitting intensity measurements. Geophys. J. Int. 210, 774–786. https://doi.org/10.1093/gji/ggx190.

Dobrosavljevic, V., Zhang, D., Sturhahn, W., Chariton, S., Prakapenka, V., Zhao, J., Toellner, T., Pardo, O., Jackson, J., 2023. Melting and defect transitions in FeO up to pressures of Earth's core-mantle boundary. Nat. Commun. https://doi.org/10.1038/s41467-023-43154-w.

Dobrosavljevic, V.V., Sturhahn, W., Jackson, J.M., 2019. Evaluating the role of iron-rich (Mg, Fe)O in ultralow velocity zones. Minerals. https://doi.org/10.3390/min9120762.

Dziewonski, A.M., Anderson, D.L., 1981. Preliminary reference Earth model. Phys. Earth Planet. Inter. 25, 297–356. https://doi.org/10.1016/0031-9201(81)90046-7.

Fernando, B., Wolf, J., Leng, K., Nissen-Meyer, T., Eaton, W., Styczinski, M., Walker, A., Craig, T., Muir, J., Nunn, C., Long, M., 2024. Axisem3D - an introduction to using the code and its applications. EarthArXiv. https://doi.org/10.31223/X5TH7P.

Ferrick, A.L., Korenaga, J., 2023. Defining Earth's elusive thermal budget in the presence of a hidden reservoir. Earth Planet. Sci. Lett. 601, 117893. https://doi.org/10.1016/j.epsl.2022.117893.

Festin, M.M., Thorne, M.S., Li, M., 2024. Evidence for ultra-low velocity zone genesis in downwelling subducted slabs at the core–mantle boundary. Seism. Rec. 4, 111–120. https://doi.org/10.1785/0320240003.

French, S.W., Romanowicz, B.A., 2014. Whole-mantle radially anisotropic shear velocity structure from spectral-element waveform tomography. Geophys. J. Int. 199, 1303–1327. https://doi.org/10.1093/gji/ggu334.

Garnero, E.J., Grand, S.P., Helmberger, D.V., 1993. Low P-wave velocity at the base of the mantle. Geophys. Res. Lett. 20, 1843–1846. https://doi.org/10.1029/93GL02009.

Garnero, E.J., Helmberger, D.V., 1998. Further structural constraints and uncertainties of a thin laterally varying ultralow-velocity layer at the base of the mantle. J. Geophys. Res., Solid Earth 103, 12495–12509. https://doi.org/10.1029/98JB00700.

Garnero, E.J., Jeanloz, R., 2000. Fuzzy patches on the Earth's core-mantle boundary? Geophys. Res. Lett. 27, 2777–2780. https://doi.org/10.1029/2000GL008498.

Garnero, E.J., Revenaugh, J., Williams, Q., Lay, T., Kellogg, L., 1998. Ultralow velocity zone at the core-mantle boundary. Geodynamics 28, 319–334. https://doi.org/10.1029/GD028p0319.

Grund, M., Ritter, J.R., 2019. Widespread seismic anisotropy in Earth's lowermost mantle beneath the Atlantic and Siberia. Geology 47, 123–126. https://doi.org/10.1130/G45514.1.

Hansen, S.E., Garnero, E.J., Li, M., Shim, S.H., Rost, S., 2023. Globally distributed subducted materials along the Earth's core-mantle boundary: implications for ultralow velocity zones. Sci. Adv. 9, eadd4838. https://doi.org/10.1126/sciadv.add4838.

Havens, E., Revenaugh, J., 2001. A broadband seismic study of the lowermost mantle beneath Mexico: constraints on ultralow velocity zone elasticity and density. J. Geophys. Res., Solid Earth 106, 30809–30820. https://doi.org/10.1029/2000JB000072.

Hein, G., Kolínský, P., Bianchi, I., Bokelmann, G., AlpArray Working Group, 2021. Shear wave splitting in the Alpine region. Geophys. J. Int. 125, 1996–2015. https://doi.org/10.1093/gji/ggab305.

Hernlund, J., Thomas, C., Tackley, P., 2005. A doubling of the post-perovskite phase boundary and structure of the Earth's lowermost mantle. Nature 434, 882–886. https://doi.org/10.1038/nature03472.

Hirose, K., Takafuji, N., Sata, N., Ohishi, Y., 2005. Phase transition and density of subducted morb crust in the lower mantle. Earth Planet. Sci. Lett. 237, 239–251. https://doi.org/10.1016/j.epsl.2005.06.035.

Hutko, A., Lay, T., Garnero, E., Revenaugh, J., 2006. Seismic detection of folded, subducted lithosphere at the core–mantle boundary. Nature 441, 333–336. https://doi.org/10.1038/nature04757.

IRIS Transportable Array, 2003. USArray transportable array. https://www.fdsn.org/networks/detail/TA/. https://doi.org/10.7914/SN/TA.

Karato, S., Jung, H., Katayama, I., Skemer, P., 2008. Geodynamic significance of seismic anisotropy of the upper mantle: new insights from laboratory studies. Annu. Rev. Earth Planet. Sci. 36, 59–95. https://doi.org/10.1146/annurev.earth.36.031207.124120.

Kendall, J.M., Silver, P., 1998. Investigating causes of D″ anisotropy. In: The Core-Mantle Boundary Region. In: Geodynamic Series, vol. 28. Core–Mantle Boundary Region, pp. 97–118.

Ko, B., Chariton, S., Prakapenka, V., Chen, B., Garnero, E.J., Li, M., Shim, S.H., 2022. Water-induced diamond formation at Earth's core-mantle boundary. Geophys. Res. Lett. 49, e2022GL098271. https://doi.org/10.1029/2022GL098271.

Labrosse, S., Hernlund, J., Coltice, N., 2008. A crystallizing dense magma ocean at the base of the Earth's mantle. Nature 450, 866–869. https://doi.org/10.1038/nature06355.

Lai, V.H., Helmberger, D.V., Dobrosavljevic, V.V., Wu, W., Sun, D., Jackson, J.M., Gurnis, M., 2022. Strong ULVZ and slab interaction at the northeastern edge of the Pacific LLSVP favors plume generation. Geochem. Geophys. Geosyst. 23, e2021GC010020. https://doi.org/10.1029/2021GC010020.

Lay, T., Garnero, E., Williams, Q., 2004. Partial melting in a thermo-chemical boundary layer at the base of the mantle. Phys. Earth Planet. Inter. 146, 441–467. https://doi.org/10.1016/j.pepi.2004.04.004.

Leng, K., Nissen-Meyer, T., van Driel, M., 2016. Efficient global wave propagation adapted to 3-D structural complexity: a pseudospectral/spectral-element approach. Geophys. J. Int. 207, 1700–1721. https://doi.org/10.1093/gji/ggw363.

Leng, K., Nissen-Meyer, T., van Driel, M., Hosseini, K., Al-Attar, D., 2019. AxiSEM3D: broad-band seismic wavefields in 3-D global Earth models with undulating discontinuities. Geophys. J. Int. 217, 2125–2146. https://doi.org/10.1093/gji/ggz092.

Lesher, C.E., Dannberg, J., Barfod, G.H., Bennett, N.R., Glessner, J.J.G., Lacks, D.J., Brenan, J.M., 2020. Iron isotope fractionation at the core-mantle boundary by thermodiffusion. Nat. Geosci. https://doi.org/10.1038/s41561-020-0560-y.

Li, M., 2020. The formation of hot thermal anomalies in cold subduction-influenced regions of Earth's lowermost mantle. J. Geophys. Res., Solid Earth 125, e2019JB019312. https://doi.org/10.1029/2019JB019312.

Li, M., 2023. Variable distribution of subducted oceanic crust beneath subduction regions of the lowermost mantle. Phys. Earth Planet. Inter. 341, 107063. https://doi.org/10.1016/j.pepi.2023.107063.

Li, M., McNamara, A., Garnero, E., Yu, S., 2017. Compositionally-distinct ultra-low velocity zones on Earth's core-mantle boundary. Nat. Commun. 177. https://doi.org/10.1038/s41467-017-00219-x.

Li, Z., Leng, K., Jenkins, J., Cottaar, S., 2022. Kilometer-scale structure on the core–mantle boundary near Hawaii. Nat. Commun., 1–8. https://doi.org/10.1038/s41467-022-30502-5.

Long, M.D., 2009. Complex anisotropy in D″ beneath the eastern Pacific from SKS–SKKS splitting discrepancies. Earth Planet. Sci. Lett. 283, 181–189. https://doi.org/10.1016/j.epsl.2009.04.019.

Long, M.D., Silver, P.G., 2009. Shear wave splitting and mantle anisotropy: measurements, interpretations, and new directions. Surv. Geophys. 30, 407–461. https://doi.org/10.1007/s10712-009-9075-1.

Loper, D.E., Lay, T., 1995. The core-mantle boundary region. J. Geophys. Res., Solid Earth 100, 6397–6420. https://doi.org/10.1029/94JB02048.

McNamara, A., van Keken, P., Karato, S., 2002. Development of anisotropic structure in the Earth's lower mantle by solid-state convection. Nature 416, 310–314. https://doi.org/10.1038/416310a.

McNamara, A.K., Garnero, E.J., Rost, S., 2010. Tracking deep mantle reservoirs with ultra-low velocity zones. Earth Planet. Sci. Lett. 299, 1–9. https://doi.org/10.1016/j.epsl.2010.07.042.

McNamara, A.K., van Keken, P.E., Karato, S., 2003. Development of finite strain in the convecting lower mantle and its implications for seismic anisotropy. J. Geophys. Res., Solid Earth 108. https://doi.org/10.1029/2002JB001970.

Meade, C., Silver, P.G., Kaneshima, S., 2005. Laboratory and seismological observations of lower mantle isotropy. Geophys. Res. Lett. 22, 1293–1296. https://doi.org/10.1029/95GL01091.

Murakami, M., Hirose, K., Kawamura, K., Sata, N., Ohishi, Y., 2004. Post-perovskite phase transition in MgSiO3. Science 304, 855–858. https://doi.org/10.1126/science.1095932.

Niu, F., Perez, A.M., 2004. Seismic anisotropy in the lower mantle: a comparison of waveform splitting of SKS and SKKS. Geophys. Res. Lett. 31. https://doi.org/10.1029/2004GL021196.

Northern California Earthquake Data Center, 2014. Berkeley digital seismic network (BDSN). https://doi.org/10.7932/BDSN.

Nowacki, A., Wookey, J., Kendall, J.M., 2010. Deformation of the lowermost mantle from seismic anisotropy. Nature 467, 1091–1094. https://doi.org/10.1038/nature09507.

Nowacki, A., Wookey, J., Kendall, J.M., 2011. New advances in using seismic anisotropy, mineral physics and geodynamics to understand deformation in the lowermost mantle. J. Geodyn. 52, 205–228. https://doi.org/10.1016/j.jog.2011.04.003.

Otsuka, K., Karato, S., 2012. Deep penetration of Molten iron into the mantle caused by a morphological instability. Nature 492, 243–246. https://doi.org/10.1038/nature11663.

Panning, M., Romanowicz, B., 2006. A three-dimensional radially anisotropic model of shear velocity in the whole mantle. Geophys. J. Int. 167, 361–379. https://doi.org/10.1111/j.1365-246X.2006.03100.x.

Reiss, M., Rümpker, G., 2017. SplitRacer: MATLAB code and GUI for semiautomated analysis and interpretation of teleseismic shear-wave splitting. Seismol. Res. Lett. 88, 392–409. https://doi.org/10.1785/0220160191.

Reiss, M.C., Long, M.D., Creasy, N., 2019. Lowermost mantle anisotropy beneath Africa from differential SKS-SKKS shear-wave splitting. J. Geophys. Res., Solid Earth 124, 8540–8564. https://doi.org/10.1029/2018JB017160.

Revenaugh, J., Meyer, R., 1997. Seismic evidence of partial melt within a possibly ubiquitous low-velocity layer at the base of the mantle. Science 277, 670–673. https://doi.org/10.1126/science.277.5326.670.

Ringwood, A., 1990. Slab-mantle interactions: 3. petrogenesis of intraplate magmas and structure of the upper mantle. Chem. Geol. 82, 187–207. https://doi.org/10.1016/0009-2541(90)90081-H.

Ritsema, J., Deuss, A., van Heijst, H.J., Woodhouse, J.H., 2011. S40RTS: a degree-40 shear-velocity model for the mantle from new Rayleigh wave dispersion, teleseismic traveltime and normal-mode splitting function measurements. Geophys. J. Int. 184, 1223–1236. https://doi.org/10.1111/j.1365-246X.2010.04884.x.

Romanowicz, B., Wenk, H.R., 2017. Anisotropy in the deep Earth. Phys. Earth Planet. Inter. 269, 58–90. https://doi.org/10.1016/j.pepi.2017.05.005.

Rondenay, S., Fischer, K.M., 2003. Constraints on localized core-mantle boundary structure from multichannel, broadband sks coda analysis. J. Geophys. Res., Solid Earth 108, 1–16. https://doi.org/10.1029/2003JB002518.

Russell, S., Irving, J.C., Cottaar, S., 2022. Seismic visibility of melt at the core-mantle boundary from PKKP diffracted waves. Earth Planet. Sci. Lett. 595, 117768. https://doi.org/10.1016/j.epsl.2022.117768.

Russell, S., Irving, J.C.E., Jagt, L., Cottaar, S., 2023. Evidence for a kilometer-scale seismically slow layer atop the core-mantle boundary from normal modes. Geophys. Res. Lett. 50, e2023GL105684. https://doi.org/10.1029/2023GL105684.

Silver, P.G., Chan, W.W., 1991. Shear wave splitting and subcontinental mantle deformation. J. Geophys. Res., Solid Earth 96, 16429–16454. https://doi.org/10.1029/91JB00899.

Simmons, N.A., Forte, A.M., Boschi, L., Grand, S.P., 2010. GyPSuM: a joint tomographic model of mantle density and seismic wave speeds. J. Geophys. Res., Solid Earth 115. https://doi.org/10.1029/2010JB007631.

Tesoniero, A., Leng, K., Long, M.D., Nissen-Meyer, T., 2020. Full wave sensitivity of SK(K)S phases to arbitrary anisotropy in the upper and lower mantle. Geophys. J. Int. 222, 412–435. https://doi.org/10.1093/gji/ggaa171.

Thorne, M.S., Leng, K., Pachhai, S., Rost, S., Wicks, J., Nissen-Meyer, T., 2021. The most parsimonious ultralow-velocity zone distribution from highly anomalous SPdKS waveforms. Geochem. Geophys. Geosyst. 22, e2020GC009467. https://doi.org/10.1029/2020GC009467.

Thorne, M.S., Pachhai, S., Leng, K., Wicks, J.K., Nissen-Meyer, T., 2020. New candidate ultralow-velocity zone locations from highly anomalous SPdKS waveforms. Minerals 10. https://doi.org/10.3390/min10030211.

Thorne, M.S., Takeuchi, N., Shiomi, K., 2019. Melting at the edge of a slab in the deepest mantle. Geophys. Res. Lett. 46, 8000–8008. https://doi.org/10.1029/2019GL082493.

Trønnes, R.G., 2010. Structure, mineralogy and dynamics of the lowermost mantle. Mineral. Petrol. 99, 243–261. https://doi.org/10.1007/s00710-009-0068-z.

UC San Diego, 1982. ANZA regional network. https://doi.org/10.7914/SN/AZ.

van der Meer, D.G., van Hinsbergen, D.J., Spakman, W., 2018. Atlas of the underworld: slab remnants in the mantle, their sinking history, and a new outlook on lower mantle viscosity. Tectonophysics 723, 309–448. https://doi.org/10.1016/j.tecto.2017.10.004.

Walsh, E., Arnold, R., Savage, M.K., 2013. Silver and Chan revisited. J. Geophys. Res., Solid Earth 118, 5500–5515. https://doi.org/10.1002/jgrb.50386.

Walter, M.J., 2021. Water transport to the core–mantle boundary. Nat. Sci. Rev. 8. https://doi.org/10.1093/nsr/nwab007.

Wessel, P., Smith, W.H.F., 1998. New, improved version of generic mapping tools released. Eos Trans. AGU 79, 579. https://doi.org/10.1029/98EO00426.

Williams, Q., Garnero, E.J., 1996. Seismic evidence for partial melt at the base of Earth's mantle. Science 273, 1528–1530. https://doi.org/10.1126/science.273.5281.1528.

Wolf, J., Frost, D.A., Long, M.D., Garnero, E., Aderoju, A.O., Creasy, N., Bozdağ, E., 2023a. Observations of mantle seismic anisotropy using array techniques: shear-wave splitting of beamformed SmKS phases. J. Geophys. Res., Solid Earth 128, e2022JB025556. https://doi.org/10.1029/2022JB025556.

Wolf, J., Li, M., Haws, A.A., Long, M.D., 2024c. Strong seismic anisotropy due to upwelling flow at the root of the Yellowstone mantle plume. Geology. https://doi.org/10.1130/G51919.1.

Wolf, J., Li, M., Long, M., Garnero, E., 2024b. Advances in mapping lowermost mantle convective flow with seismic anisotropy observations. Rev. Geophys. https://doi.org/10.1029/2023RG000833.

Wolf, J., Long, M.D., 2022. Slab-driven flow at the base of the mantle beneath the northeastern Pacific Ocean. Earth Planet. Sci. Lett. 594, 117758. https://doi.org/10.1016/j.epsl.2022.117758.

Wolf, J., Long, M.D., 2023. Lowermost mantle structure beneath the central Pacific Ocean: ultralow velocity zones and seismic anisotropy. Geochem. Geophys. Geosyst. 24, e2022GC010853. https://doi.org/10.1029/2022GC010853.

Wolf, J., Long, M.D., Creasy, N., Garnero, E., 2023b. On the measurement of Sdiff splitting caused by lowermost mantle anisotropy. Geophys. J. Int. https://doi.org/10.1093/gji/ggac490.

Wolf, J., Long, M.D., Frost, D.A., 2024a. Ultralow velocity zone and deep mantle flow beneath the Himalayas linked to subducted slab. Nat. Geosci. https://doi.org/10.1038/s41561-024-01386-5.

Wolf, J., Long, M.D., Leng, K., Nissen-Meyer, T., 2022. Constraining deep mantle anisotropy with shear wave splitting measurements: challenges and new measurement strategies. Geophys. J. Int., 507–527. https://doi.org/10.1093/gji/ggac055.

Wolf, J., Long, M.D., Li, M., Garnero, E., 2023c. Global compilation of deep mantle anisotropy observations and possible correlation with low velocity provinces. Geochem. Geophys. Geosyst. 24, e2023GC011070. https://doi.org/10.1029/2023GC011070.

Yamazaki, D., Karato, S., 2007. Lattice-preferred orientation of lower mantle materials and seismic anisotropy in the D″ layer. In: Geophysical Monograph Series. American Geophysical Union, Washington, DC, pp. 69–78.

Yu, S., Garnero, E.J., 2018. Ultralow velocity zone locations: a global assessment. Geochem. Geophys. Geosyst. https://doi.org/10.1002/2017GC007281.